Infrared spectroscopy of the benzylium-like (and tropylium-like) isomers formed in the -H dissociative ionization of methylated PAHs

Gabi Wenzel, Aude Simon, Shreyak Banhatti, Pavol Jusko, Stephan Schlemmer, Sandra Brünken, Christine Joblin

Gabi Wenzel, Aude Simon, Shreyak Banhatti, Pavol Jusko, Stephan Schlemmer, et al.. Infrared spectroscopy of the benzylium-like (and tropylium-like) isomers formed in the -H dissociative ionization of methylated PAHs. Journal of Molecular Spectroscopy, 2022, 385, 10.1016/j.jms.2022.111620 . insu-03672040

Infrared spectroscopy of the benzylium-like (and tropylium-like) isomers formed in the –H dissociative ionization of methylated PAHs

Gabi Wenzel[a,1], Aude Simon[b], Shreyak Banhatti[c], Pavol Jusko[a,2], Stephan Schlemmer[c], Sandra Brünken[d], Christine Joblin[a,*]

[a] *Institut de Recherche en Astrophysique et Planétologie (IRAP), Université Toulouse III - Paul Sabatier, CNRS, CNES, 9 Avenue du Colonel Roche, 31028 Toulouse, France*
[b] *Laboratoire de Chimie et Physique Quantiques (LCPQ), Fédération FeRMI, CNRS & Université Toulouse III - Paul Sabatier, 118 Route de Narbonne, 31062 Toulouse, France*
[c] *I. Physikalisches Institut, Universität zu Köln, Zülpicher Straße 77, 50937 Köln, Germany*
[d] *Radboud University, Institute for Molecules and Materials, FELIX Laboratory, Toernooiveld 7, 6525ED Nijmegen, The Netherlands*

Abstract

Cationic benzylium and tropylium are known to be two competitive isomers for the –H fragment of the methylbenzene (toluene) cation. Methylated polycyclic aromatic hydrocarbon (PAH) cations are expected to be abundant in space and their dehydrogenation could lead to the formation of both the benzylium- and tropylium-like cations, which are expected to be the two lowest-energy isomers. Here, we considered 1-methylpyrene and two less compact acene-substituted species, namely 2-methylnaphthalene and 2-methylanthracene, as precursors. The cationic –H fragments, $C_{17}H_{11}^+$, $C_{11}H_9^+$, and $C_{15}H_{11}^+$, were produced by dissociative ionization, and their neon tagged complexes were formed in the 22-pole cryogenic ion trap instrument FELion that is coupled to the FELIX free electron laser. Infrared (IR) predissociation spectroscopy was performed showing that the strongest depletion band is located at about 1620 cm^{-1}, which reveals the predominance of the benzylium-like, XCH_2^+, isomers, where X = Pyr, Nap, or Ant. Saturation depletion measurements showed that only this isomer is present in the case of $C_{17}H_{11}^+$, whereas for the acene-derived species at least two are present with a large abundance. Synthetic spectra were generated from the theoretical anharmonic IR spectra of the two lowest-energy isomers, namely XCH_2^+ and the tropylium-like isomers, XC_7^+. Spectral comparison led us to conclude that there is no evidence for $PyrC_7^+$ but clear evidence for $NapC_7^+$. No specific spectral features could be identified for $AntC_7^+$ due to a high spectral congestion. These results support the important role of PAH compactness in preventing the formation of XC_7^+ species. They also reveal the potential of XCH_2^+ species to account for the aromatic infrared band observed in emission at 6.2 μm in astrophysical environments.

Keywords: `Infrared predissociation spectroscopy, Polycyclic aromatic hydrocarbons, Cryogenic ion trap, Free electron laser, Quantum chemistry, Astrochemistry`

---

1. Introduction

Polycyclic aromatic hydrocarbons (PAHs) are a major component of matter in interstellar photodissociation regions (PDRs). In these regions, these species absorb ultraviolet (UV) photons, which results in emission in the aromatic infrared bands (AIBs) (see [1] for a review). Exposure to UV photons also leads to a photo-chemical evolution of the emitting populations. From the analysis of the spatial distribution of the AIB emission at the surface of dense molecular clouds, the presence of three main populations was proposed, consisting of PAH neutrals and cations as well as their precursors called evaporating very small grains (eVSGs) [2–

---

[*] Corresponding author.
Email address: `christine.joblin@irap.omp.eu` (Christine Joblin)

[1] Currently at Center for Interstellar Catalysis (InterCat), Department of Physics and Astronomy, Aarhus University, Ny Munkegade 120, 8000 Aarhus C, Denmark

[2] Currently at Max-Planck-Institut für extraterrestrische Physik, Gießenbachstraße 1, 85748 Garching, Germany

Preprint submitted to Journal of Molecular Spectroscopy *October 24, 2022*

4]. The variation of the PAH charge was rationalized by models that describe the competition between photoionization and recombination with electrons [5–7]. However, the view that we have on the chemistry in the transition zone between eVSG and PAH emissions is very limited. Pilleri et al. [8] have shown that eVSGs have a mixed aromatic and aliphatic composition and concluded that their interaction with UV photons leads to the production of gas-phase PAHs with attached aliphatic sidegroups that have a characteristic emission band at $3.4\,\mu$m [9–12].

Methyl sidegroups attached to aromatics are also expected to be common in primitive matter of the Solar System. The Rosetta Orbiter Spectrometer for Neutral and Ion Analysis (ROSINA) detected toluene in comet 67P/Churyumov-Gerasimenko [13]. Small methylated PAHs are found to be a major component in primitive carbonaceous chondrites [14–17]. Their presence indicates formation conditions at lower temperatures compared to regular PAHs [18]. Several authors also point to a growth chemistry involving an efficient methyl addition/cyclization mechanism [19–21]. The H abstraction of the methyl sidegroup followed by addition of a methyl radical would form an ethyl sidegroup that could eventually lead to cyclization into a cyclopentafused ring.

The main dissociation pathway of methylated PAHs upon irradiation by vacuum UV photons involves H loss and this occurs independently of the PAH size [22, 23]. Much earlier, Dunbar [24] discussed on the nature of the fragment $C_7H_7^+$ produced by photodissociation of the toluene cation. In experiments, two forms are observed, one which is reactive and one non-reactive. Dunbar [24] proposed that the former corresponds to the benzylium structure whereas the latter corresponds to the tropylium structure which are both depicted in Fig. 1 (a). Using metadynamics simulations, Rapacioli et al. [25] investigated isomerization pathways for the –H fragment of the 1-methylpyrene cation, $C_{17}H_{11}^+$. They found several pathways with a barrier of $3.5 - 4\,$eV between the benzylium-like methylenepyrene, $PyrCH_2^+$, and the tropylium-like $PyrC_7^+$ isomers (see structures in Fig. 1 (b)). They concluded that both isomers could co-exist in UV-irradiated astrophysical environments.

When probing such species experimentally in the gas-phase to obtain information on their structures, infrared multiple photon dissociation (IRMPD) spectroscopy is the commonly used technique. While it was demonstrated that IRMPD is a good choice for species with low dissociation thresholds, as for example in the case of the two related $C_8H_9^+$ isomers [26], the IRMPD spectra of $C_7H_7^+$ isomers are still lacking, either due to their increased stability, *i.e.*, higher dissociation thresholds compared to $C_8H_9^+$, or due to isomerization effects during infrared (IR) photon irradiation. In a previous study, Jusko et al. [27] demonstrated the potential of infrared predissociation (IRPD) spectroscopy of Ne-tagged $C_7H_7^+$ together with saturation depletion measurements in order to quantify the relative populations of benzylium and tropylium cations as a function of their formation conditions. In contrast to IRMPD, IRPD involves the absorption of only one single IR photon and, therefore, will never lead to a significant increase of energy that could alter (isomerize) the probed species. Accordingly, IRPD bands are typically much narrower and often only limited by the laser bandwidth, whereas IRMPD leads to substantial band-broadening. This is a major advantage, when the spectral assignment of individual stable isomers is searched for.

In the case of the –H fragment of the 1-methylpyrene cation it was demonstrated that the more standard IRMPD technique cannot be used to record a comprehensive spectrum of these species and discuss band assignment [28]. The latter article concluded that the main isomer formed in the experiments was $PyrCH_2^+$. However, the reported spectrum was of low signal-to-noise ratio and a relevant upper limit for the $PyrC_7^+$ species could not be derived. A recent study concluded that $PyrC_7^+$ is not expected to be formed in unimolecular dissociation of 1-methylpyrene cations because of steric effects imposed by the compactness of the molecule [29].

In this work, we extend the IRPD measurements to small acenes, namely the cationic –H fragments of 2-methylnaphthalene and 2-methylanthracene, for which we expect less energy to isomerize compared to the case of the –H fragment of the more compact 1-methylpyrene cation. We also improve the measurements on the latter cation relative to our previous study [28]. In Sect. 2, we describe our methods. This is followed by the presentation of the recorded IRPD spectra and saturation depletion measurements in Sect. 3. A spectral analysis is presented by comparison with calculated anharmonic IR spectra. In Sect. 4, we discuss the main unsolved issues in the spectral analysis, summarize our findings, and provide some astrophysical implications. We conclude in Sect. 5.

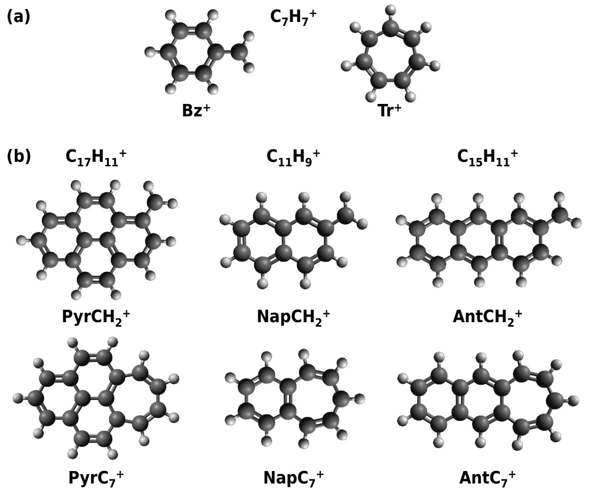

Figure 1: (a) Optimized geometries at the B3LYP/cc-pvdz level of theory of the benzylium, Bz^+, and tropylium, Tr^+, cations taken from Jusko et al. [27]. (b) Expected lowest-energy isomers resulting from H loss of cationic methylated PAHs (1-methylpyrene, 2-methylnaphthalene, and 2-methylanthracene from left to right): benzylium-like isomers with a CH_2 group attached resulting from direct H loss (top row) and tropylium-like isomers incorporating the C_7 ring (bottom row) resulting from isomerization prior to H loss. The reported geometries were optimized at the B3LYP/6-31G(d,p) level of theory.

2. Methods

2.1. Experimental

IRPD spectra of the Ne-tagged cationic –H fragments of three different methylated PAH precursors were recorded using the FELion cryogenic ion trap instrument available at the FELIX[3] Laboratory. FELion is a custom-built, cryogenically cooled 22-pole ion trap which is described in detail in Jusko et al. [30] and coupled to the free electron laser FELIX-2 [31]. The precursor species, namely 1-methylpyrene, $C_{17}H_{12}$, 2-methylnaphthalene, $C_{11}H_{10}$, and 2-methylanthracene, $C_{15}H_{12}$, are all commercially available (Sigma-Aldrich, $\geq 97.0\,\%$ purity for all three species) and were vaporized into the FELion ion source. The cationic –H fragments, *i.e.*, $C_{17}H_{11}^+$, $C_{11}H_9^+$, and $C_{15}H_{11}^+$, are directly produced by dissociative ionization of the corresponding neutral precursor by electron impact in the ion source. Due to technical reasons and beamtime management, the $C_{15}H_{11}^+$ species were efficiently produced in an RF storage source [32] with an electron impact energy of 18.0 eV, while we used a non-storage electron impact ionization source [33] for the production of $C_{17}H_{11}^+$ and $C_{11}H_9^+$ with electron impact energies of 56.7 eV and 17.0 eV, respectively. Electron impact ionization of PAHs was found to be in qualitative agreement with their respective photoionization yields [33]. No significant qualitative differences in the recorded IRPD spectra with varying ionization conditions induced by tuning the electron impact energy were observed. The –H fragments were mass-selected and guided into the 22-pole cryogenic ion trap which is mounted on a cold head cooling the trap down to a temperature of approximately 6 K to ensure efficient noble gas tagging in the trap. Upon ion injection, high quantities of a 3:1 He:Ne gas mixture were introduced into the ion trap in order to promote ternary Ne atom attachment to the cationic –H fragment species. Proof of efficient Ne tagging was given by recording the mass spectra which show the –H fragments at their respective mass-to-charge ratio, m/z, together with their Ne-tagged complexes positioned at a mass shift of $m/z = +20$ corresponding to the mass of one Ne atom with a tagging efficiency of approximately $10\,\%$ (see Fig. S1 in the Supplementary Material (SM)). The Ne-tagged complexes were stored in the 22-pole cryogenic ion trap for typically 1.6 s and irradiated by the FELIX-2 laser in the mid-IR. The depletion of these weakly bound complexes is then induced by a single photon absorption process and was recorded as a function of the FELIX-2 laser wavenumber in the range of approximately $650 - 1700\,\mathrm{cm}^{-1}$ ($15.38 - 5.88\,\mu$m) yielding the IRPD spectra. For IRPD measurements, FELIX-2 delivers between 3 and 30 mJ into the 22-pole ion trap in a single macropulse with a pulse duration of about $5\,\mu$s at a 10 Hz repetition rate. The experimental spectra, so-called depletion spectra, were normalized to FELIX-2 laser energy and baseline corrected following the procedure presented by Brünken et al. [34]. Saturation depletion measurements were performed on resonance bands for each of the complexes in order to determine isomeric ratios, the amplitude of the decay curve providing the fraction of the specific isomer(s) associated with a given resonant band. For this, the laser

---

[3] Free Electron Lasers for Infrared eXperiments, `https://www.ru.nl/felix`.

is tuned on resonance and off resonance with the vibrational band of interest. By applying a large number of photon pulses on resonance, the optically active isomer-Ne complex can be dissociated completely leaving only the optically inactive isomer-Ne complex in the trap. Recording the ion-Ne depletion

$$D(E_\mathrm{d}) = 1 - \frac{N_\mathrm{on}(E_\mathrm{d})}{N_\mathrm{off}(E_\mathrm{d})} \approx A\left(1 - \mathrm{e}^{-kE_\mathrm{d}}\right), \quad (1)$$

as a function of deposited laser energy, E_d, where $N_\mathrm{on}(E)$ and $N_\mathrm{off}(E)$ are the number of ion-Ne complexes on and off resonance, respectively, reveals the relative abundance

$$A = \frac{N_\mathrm{a}}{N_\mathrm{a} + N_\mathrm{n}} \quad (2)$$

of active (N_a) to inactive (N_n) isomers with k being the dissociation rate of the active isomer. Care has to be taken to choose vibrational bands associated with only one active isomer, *i.e.*, to avoid line blending, and in the case were more than two active isomers are present. In these cases, saturation depletion measurements on many different vibrational bands need to be performed. This technique is discussed in detail by Jusko et al. [30] and Marimuthu et al. [35].

2.2. Computational

In order to investigate the possible isomers that could form from the methylated cationic PAHs H loss, we performed molecular dynamics (MD) / density functional based tight binding (DFTB) simulations using a similar procedure as in a previous study by Joblin et al. [36]. These simulations were run with the deMonNano code [37].

Structural and energetic data for the two lowest-energy isomers determined from these simulations were obtained using density functional theory (DFT) with the hybrid functional B3LYP as implemented in the Gaussian16 suite of programs [38]. The harmonic spectra of the optimized structures were obtained by full diagonalization of the Hessian matrix. Anharmonic spectra were computed using the perturbative approach (VPT2) [39] as implemented in Gaussian16. Geometry optimization followed by harmonic and perturbative anharmonic vibrational calculations were also performed using the large def2TZVPP [40] basis set. Insights into the dependence of the theoretical spectra on functionals and basis sets were also undertaken. The energetics of the reaction paths leading to H loss from cationic 2-methylnaphthalene was investigated with the B3LYP functional using the double-ζ basis set 6-31G(d,p) with further confirmation of the energetics by single point CCSD(T)/6-311G(d,p)//B3LYP/6-31G(d,p) calculations. The nature of the transition states was confirmed by intrinsic reaction coordinate (IRC) calculations. Energetic data for the relevant intermediates were also computed for cationic 2-methylanthracene and 1-methylpyrene.

2.3. Spectral analysis

Identification of the possible isomers in the ion trap is performed by comparing the experimentally obtained IRPD spectra to the theoretically calculated anharmonic IR spectra of the selected isomeric structures. The latter were convolved with a Gaussian function of width of $\sigma = 0.3\,\%$ representing the approximate laser line profile. By this comparison, we aim at assigning bands present in the IRPD spectra to resonance bands of one or more specific isomers.

Fundamental and combination bands calculated for each considered isomer structure have the strongest intensity contribution (see Tables S1, S2, and S3 in the SM) and are therefore included in the anharmonic IR spectra. All these bands overlap and blend with each other, resulting into congested spectra. The experimental spectra present a similar complexity making a detailed analysis of the band characteristics (positions, intensities, and widths) quite challenging. In order to derive band characteristics without a multi-component analysis, we are following the procedure introduced by Chakraborty et al. [41]. The authors determined intensity-weighted band positions and widths by selecting an interval $[\nu_i^\mathrm{min}, \nu_i^\mathrm{max}]$ around each observed band, i. The mean band positions and widths, $\bar{\nu}_i$ and σ_i, respectively, are defined in the following equations as

$$\bar{\nu}_i = \frac{\int_{\nu_i^\mathrm{min}}^{\nu_i^\mathrm{max}} \nu I(\nu)\,\mathrm{d}\nu}{\int_{\nu_i^\mathrm{min}}^{\nu_i^\mathrm{max}} I(\nu)\,\mathrm{d}\nu} = \frac{1}{I_i}\int_{\nu_i^\mathrm{min}}^{\nu_i^\mathrm{max}} \nu I(\nu)\,\mathrm{d}\nu, \quad (3)$$

where $I(\nu)$ is the band intensity as a function of wavenumber, ν, I_i is the integrated intensity of band i, and

$$\sigma_i = \sqrt{\frac{1}{I_i}\int_{\nu_i^\mathrm{min}}^{\nu_i^\mathrm{max}} (\nu - \bar{\nu}_i)^2 I(\nu)\,\mathrm{d}\nu}. \quad (4)$$

This method can be applied to the experimental IRPD spectra and the calculated anharmonic IR spectra in the same way. To quantify the comparison between both types of spectra, we introduce the difference between their weighted band positions as

$$\Delta\bar{\nu}_i = \bar{\nu}_i^{\mathrm{ex}} - \bar{\nu}_i^{\mathrm{th}}, \tag{5}$$

where $\bar{\nu}_i^{\mathrm{ex}}$ denotes the experimental and $\bar{\nu}_i^{\mathrm{th}}$ the theoretical anharmonic weighted band position for band i.

3. Results

3.1. IRPD spectra

The recorded IRPD spectra of the cationic –H fragments, $C_{17}H_{11}^+$, $C_{11}H_9^+$, and $C_{15}H_{11}^+$, are presented in Fig. 2. After correction for FELIX-2 laser power and baseline subtraction, the IRPD spectra are in relative units ($\sim$ m^2/photon, see Brünken et al. [34]) and comparable with each other. In these relative units, the peak intensity of the most prominent band is the strongest for $C_{17}H_{11}^+$; it decreases by approximately 30 % for $C_{11}H_9^+$ and by another approximately 20 % for $C_{15}H_{11}^+$. In the following, the IRPD spectra presented in Figs. 4, 5, and 6 were normalized to unity at the maximum peak, which is observed in the 1600 cm^{-1} range for all species. Comparing our spectra to the IRPD spectra of benzylium and tropylium, $C_7H_7^+$ [27], we allocate this band to be dominated by the contribution of the benzylium-like methylene structures.

While the IRPD spectrum of the compact pyrene-like $C_{17}H_{11}^+$ is dominated by a set of narrow and well-defined depletion bands, a higher spectral congestion is observed for the acene-derived structures, $C_{11}H_9^+$ and $C_{15}H_{11}^+$. This may indicate a larger isomer diversity for these ions. Band overlaps are especially prominent in the $1320 - 1480$ cm^{-1} region.

The lower frequency region below 1100 cm^{-1} is dominated by a single band due to overlapping CH out-of-plane bending modes for $C_{17}H_{11}^+$. The acene-derived structures, however, depict more bands that are better resolved for the $C_{11}H_9^+$ case. For $C_{15}H_{11}^+$, the main band is broadened, suggesting the contribution of at least two components.

3.2. Saturation depletion measurements

Two resonance bands per cationic –H fragment were selected to perform saturation depletion measurements. The corresponding band positions are indicated in Fig. 2 with band numbers (1) – (6). Background measurements were performed off resonance for each species. The depletion data can be fitted with an exponential decay as a function of deposited laser energy, $D(E_\mathrm{d})$, following the procedure discussed in [30, 35] with

$$D(E_\mathrm{d}) = 1 - \frac{S}{B} \approx A\left(1 - \mathrm{e}^{-kE_\mathrm{d}}\right), \tag{6}$$

where S denotes the signal on a resonance band and B off resonance (background position), k is the decay rate of the active isomer, *i.e.*, the isomer that absorbs in the selected resonance band, and A is the relative abundance of this active isomer in the trap. The saturation depletion time scans and fitted depletion for bands $(1) - (6)$ are shown in Fig. 3.

In the case of $C_{17}H_{11}^+$, depletion saturation measurements were carried out on band (1) at 1379 cm^{-1} and on band (2) at 1620 cm^{-1} relative to the background positioned at 1668 cm^{-1}. Comparing the relative abundances with each other, we seem to have picked resonance bands of the same active isomer, as A yields (96 ± 2) % on band (1) and (95 ± 1) % on band (2).

For the smaller $C_{11}H_9^+$, distinct narrow bands that did not seem to have major overlaps with others were observed mostly in the $750 - 850$ cm^{-1} range. The saturation depletion time scans were performed on the resonance bands (3) at 791 cm^{-1} and (4) at 818 cm^{-1} relative to off resonance at 850 cm^{-1}, yielding isomer abundances of (40 ± 8) % and (74 ± 5) %, respectively. These percentages only agree on the lower limit of the error with each other and therefore give only a rough estimate of the isomer mixture, perhaps due to partial overlap of one or both bands with others.

The $C_{15}H_{11}^+$ spectrum exhibits only two somewhat narrow bands that are located in two different regions of the spectrum (see Fig. 2, bottom panel), band (5) at 756 cm^{-1} and band (6) at 1519 cm^{-1}. Due to the large spectral difference of these bands, two different background off resonance time scans were recorded at 738 cm^{-1} and 1540 cm^{-1} for band (5) and (6), respectively. The depletion fits resulted in abundances of the active isomer of (74 ± 3) % and (67 ± 5) % on band (5) and band (6), respectively. The similar abundance values of the depletion saturation measurements could account for selecting resonance bands of the same isomer, or for a mixture of isomers with blended bands.

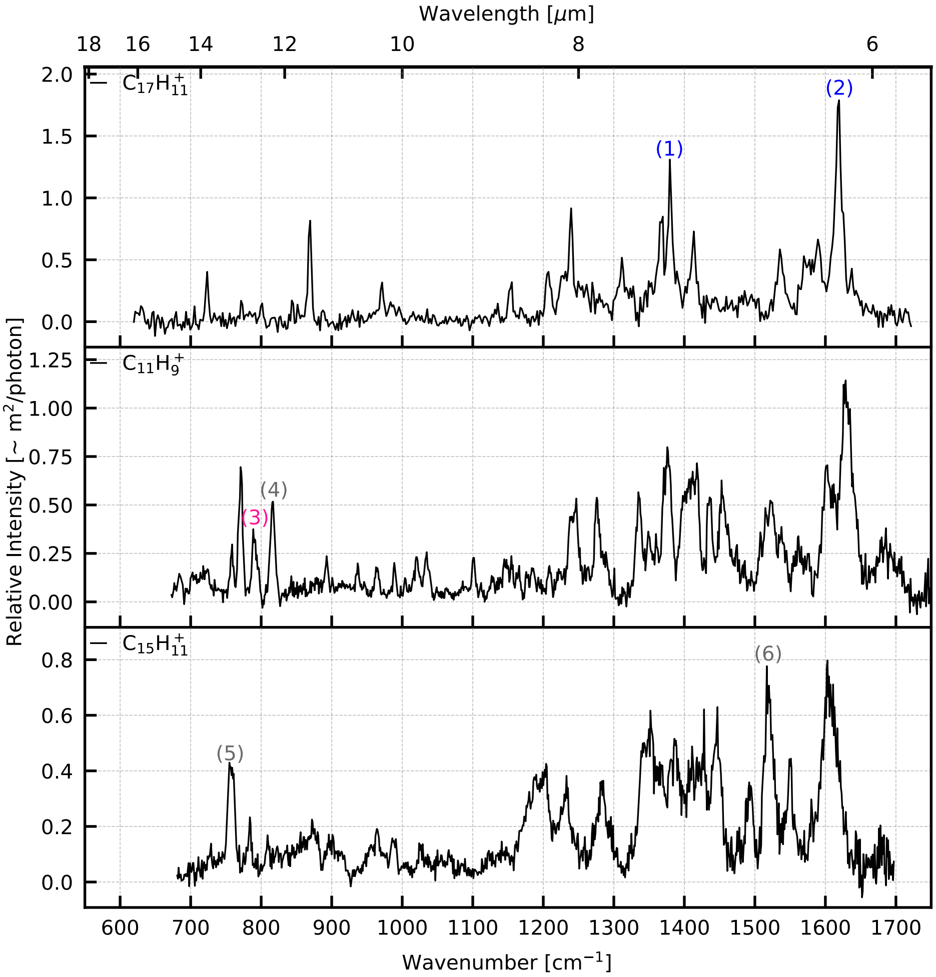

Figure 2: Experimental IRPD spectra of Ne-tagged $C_{17}H_{11}^+$ (top), $C_{11}H_9^+$ (middle), and $C_{15}H_{11}^+$ (bottom). Saturation depletion measurements performed on specific resonance bands are marked with numbers, *i.e.*, (1) – (6).

3.3. Spectral and structural assignment

MD/DFTB simulations allowed the identification of several isomers that could form after H loss from 2-methylnaphthalene, $NapCH_3^+$ (see Sect. ‘Exploration of isomer diversity by MD simulations’ in the SM). The structures of all obtained isomers were further reoptimized at the B3LYP/6-31G(d,p) level of theory, confirming the energetic order provided by DFTB (see Fig. S2 in the SM). In particular, we confirmed that the two lowest-energy isomers were indeed the benzylium-like $NapCH_2^+$ and the tropylium-like $NapC_7^+$ structures (see Fig. 1 (b) for their structures), to the precision of the calculations. At the DFT level, $NapC_7^+$ $^1A_1$ (C_{2v} group) was found to be more stable than $NapCH_2^+$ $^1A'$ (C_s group) by 0.31 eV (0.25 eV at the CCSD(T) level). Similarly, we assumed that two equivalent structures were formed in the case of both the 1-methylpyrene and the 2-methylanthracene precursor species as invoked in previous studies [25, 28, 29]. All structures were found to belong to the C_s symmetry group and have $^1A'$ electronic ground states except $AntC_7^+$ which, similarly to $NapC_7^+$, belongs to the C_{2v} symmetry group and has a $^1A_1$ electronic ground state. We found that $AntC_7^+$ was 0.23 eV below $AntCH_2^+$ (0.17 eV at the CCSD(T) level) while $PyrCH_2^+$ and $PyrC_7^+$ were found quasi-degenerate in previous work [25]. All resulting optimized geometries are reported in Fig. 1 (b).

Theoretical anharmonic IR spectra for these six structures were calculated using the B3LYP functional in combination with the 6-311G(d,p) and the def2TZVPP basis sets. Comparing these spectra with each other illustrates the impact of the basis

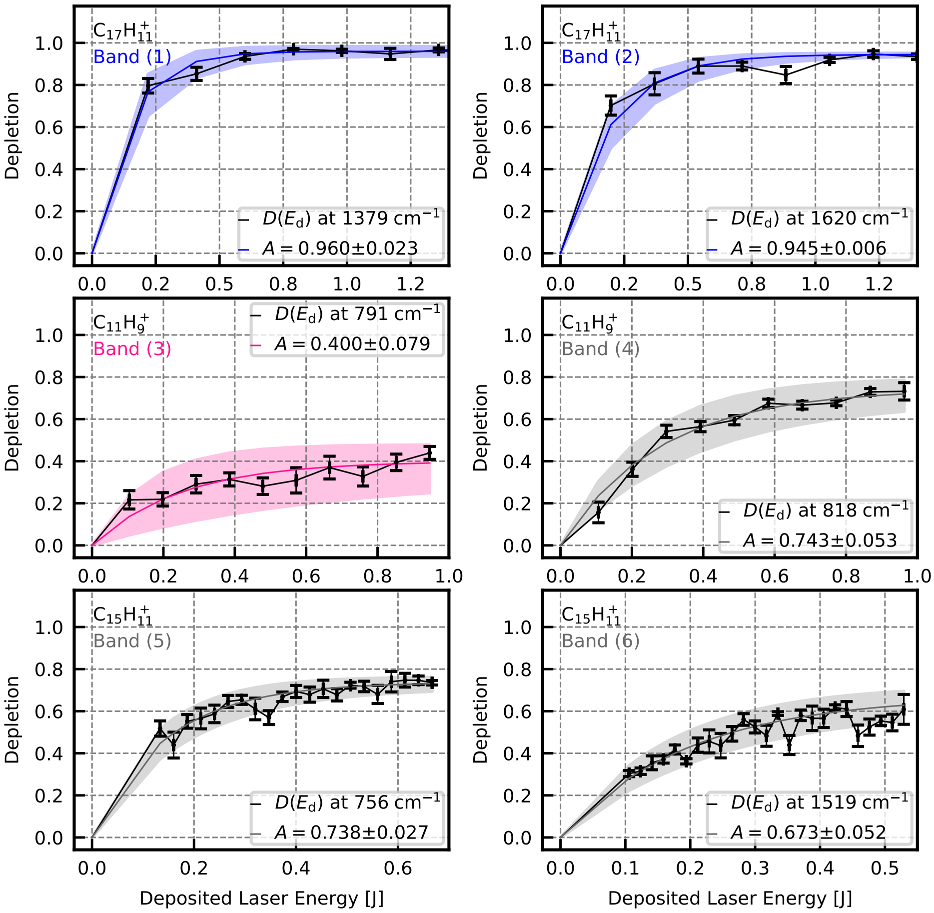

Figure 3: Saturation depletion, D, measured as a function of deposited laser energy, E_{d}, on the six recorded band positions, (1) – (6), as marked in the respective experimental IRPD spectra presented in Fig 2. The colors represent the assigned isomer, blue for the XCH_2^+ species, pink for the XC_7^+ species and, gray unassigned (see Sect. 3.3 for details).

set on the anharmonic spectra (see Sect. 'Comparison of basis sets def2TZVPP and 6-311G(d,p)' and Figs. S3, S4, and S5 in the SM). Interestingly, comparing the positions of the fundamental anharmonic *vs.* harmonic resonant modes, the former are shifted towards lower energy with respect to the latter and the values of the shifts (typically $-40\,\mathrm{cm}^{-1}$ for the bands at $1600\,\mathrm{cm}^{-1}$) correspond to the common scaling factors used for harmonic spectra of PAHs (0.975 in this case). In the following, we use the anharmonic spectra obtained with the largest basis set, *i.e.*, def2TZVPP.

The IRPD spectra of the Ne-tagged $C_{17}H_{11}^+$, $C_{11}H_9^+$, and $C_{15}H_{11}^+$ are reported in the top panels of Figs. 4, 5, and 6, respectively. They are displayed together with the computed anharmonic IR spectra corresponding to their respective XCH_2^+ (middle panel) and XC_7^+ (bottom panel) isomers, where X = Pyr, Nap, and Ant. It is obvious from the comparison of the theoretical spectra with the experimental ones that the dominant isomer is in all cases XCH_2^+, whereas XC_7^+ has a more minor contribution. To compare further the experimental and theoretical spectra, we used the saturation depletion values that were determined in Sect. 3.2. At a first glance, we can consider these values as representatives of isomer abundance ratios, with a typical value of 5 % for $PyrC_7^+$ and 30 % for the other XC_7^+ species. Multiplying the theoretical anharmonic IR spectrum of each isomer with its respective relative abundance factor and summing them yields one synthetic IR spectrum per –H fragment species. To facilitate the comparison of the synthetic spectra with the experimental spectra, we scaled the former to the latter by using the integrated intensity in the $650 - 1700\,\mathrm{cm}^{-1}$ range. The resulting synthetic anharmonic IR spectra are depicted in the top panels of Figs. 4, 5, and 6 and can now be directly compared to our experimental IRPD spectra.

Due to the spectral congestion, we will use, in order to quantify the match between the experimental and synthetic spectra, the intensity-weighted band positions and widths and the corresponding band integrated intensities as defined in Eqs. (3) and (4) of Sect. 2.3. The results are summarized in Table 1 for all considered species together with the band position difference, $\Delta\bar{\nu}_i$, defined by Eq. (5).

We note a good agreement in band positions between the experimental and synthetic spectra as $|\Delta\bar{\nu}_i| < 10\,\mathrm{cm}^{-1}$ for all but one major band of $\mathrm{C_{17}H_{11}^+}$. After the scaling procedure discussed above, the integrated intensities, I_i, are also comparable within a factor of approximately 2 for a large number of the bands. Significant discrepancies are noted though for the bands at 723 and $1581\,\mathrm{cm}^{-1}$ for $\mathrm{C_{17}H_{11}^+}$, 770, 1243, 1336, 1603, and $1633\,\mathrm{cm}^{-1}$ for $\mathrm{C_{11}H_9^+}$, and 1285 and $1551\,\mathrm{cm}^{-1}$ for $\mathrm{C_{15}H_{11}^+}$.

In the case of $\mathrm{C_{17}H_{11}^+}$, the strongest band observed at $1622\,\mathrm{cm}^{-1}$ only shows a $-1\,\mathrm{cm}^{-1}$ shift to its theoretical counterpart and the integrated intensities match well with each other. This is also one of the resonance bands on which saturation depletion measurements were performed, band (2), and which we assigned to $\mathrm{PyrCH_2^+}$. The other resonance band, band (1), is the one with the largest $\Delta\bar{\nu}_i = 12\,\mathrm{cm}^{-1}$ reported, but due to the similarity in the saturation depletion measurement abundance value (see Sect. 3.2), we assign also this band to $\mathrm{PyrCH_2^+}$. This becomes especially clear when comparing to the intensities of the anharmonic IR spectrum of $\mathrm{PyrC_7^+}$ (see Fig. 4 (bottom panel) and Table S1 in the SM) which are too low to explain the strong bands observed in the IRPD spectrum of $\mathrm{C_{17}H_{11}^+}$, whereas the strongest bands of the IR spectrum of $\mathrm{PyrC_7^+}$ cannot be observed in the measured spectrum. However, from the reported band position difference and the saturation depletion measurements, we cannot exclude a contribution of $\mathrm{PyrC_7^+}$ to the IRPD spectrum, with a 5 % upper limit for the relative abundance.

For the smallest investigated species, $\mathrm{C_{11}H_9^+}$, we concentrate on the low frequency region in which narrow, distinct bands can be observed in the IRPD spectrum reported in Fig. 5 and on which saturation depletion measurements were performed. From these, we deduce that in order to explain the depletion abundance values, a mixture consisting of at least two abundant isomers is present in the ion trap. Due to the $\Delta\bar{\nu}_i = 5\,\mathrm{cm}^{-1}$ and the excellent agreement between the I_i values of the IRPD and the synthetic spectra, we attribute the band (3) at $791\,\mathrm{cm}^{-1}$ to $\mathrm{NapC_7^+}$. The saturation depletion measurement yielded a value of about 40 %, which would correspond to a maximum relative abundance of 40 % for $\mathrm{NapC_7^+}$. For band (4) at $816\,\mathrm{cm}^{-1}$, the band position shift is of $7\,\mathrm{cm}^{-1}$, but the integrated intensity differs by a factor of 2. Here we cannot clearly assign this band to one or the other isomer and it might result from a blending of bands of both. The situation is different for the higher wavenumber region around and above $1600\,\mathrm{cm}^{-1}$. As previously mentioned, we assign the strongest observed IRPD band at $1633\,\mathrm{cm}^{-1}$ to be dominated by the benzylium-like isomer, $\mathrm{NapCH_2^+}$. However, we also observe a shoulder on the red side of this band which we found to be centered at $1603\,\mathrm{cm}^{-1}$ and that could be associated with the $\mathrm{NapC_7^+}$. We thus conclude that both stable isomers are abundant.

In the case of $\mathrm{C_{15}H_{11}^+}$, none of the observed bands in the IRPD spectrum can be assigned clearly to one isomer or the other. This is because both anharmonic IR spectra of $\mathrm{AntCH_2^+}$ and $\mathrm{AntC_7^+}$ depict features in the same regions and these all seem to overlap in the recorded IRPD spectrum. Even the strong band at $1606\,\mathrm{cm}^{-1}$ has an anharmonic fundamental band counterpart in the IR spectrum of $\mathrm{AntC_7^+}$ (see Table S3 in the SM). Isomer mixing is also present for the two bands on which we performed saturation depletion measurements, band (5) and (6) at $756\,\mathrm{cm}^{-1}$ and $1519\,\mathrm{cm}^{-1}$, respectively. In this context, it is difficult to assign the approximately 70 % abundance deduced for both resonance bands. It is related to $\mathrm{AntCH_2^+}$ or a mixture of $\mathrm{AntCH_2^+}$ and $\mathrm{AntC_7^+}$, but in this case, it means that we are missing one or several other isomers at the level of 30 % abundance.

4. Discussion

4.1. Spectral assignment discussion

As discussed in Sect. 1, IRPD is expected to be the technique of choice to probe a mixture of isomers. In the case of $\mathrm{C_{17}H_{11}^+}$, the recorded IRPD spectrum can be explained by a largely dominant contribution of the $\mathrm{PyrCH_2^+}$ isomer. In the case of the acene-derived species, the spectra exhibit more

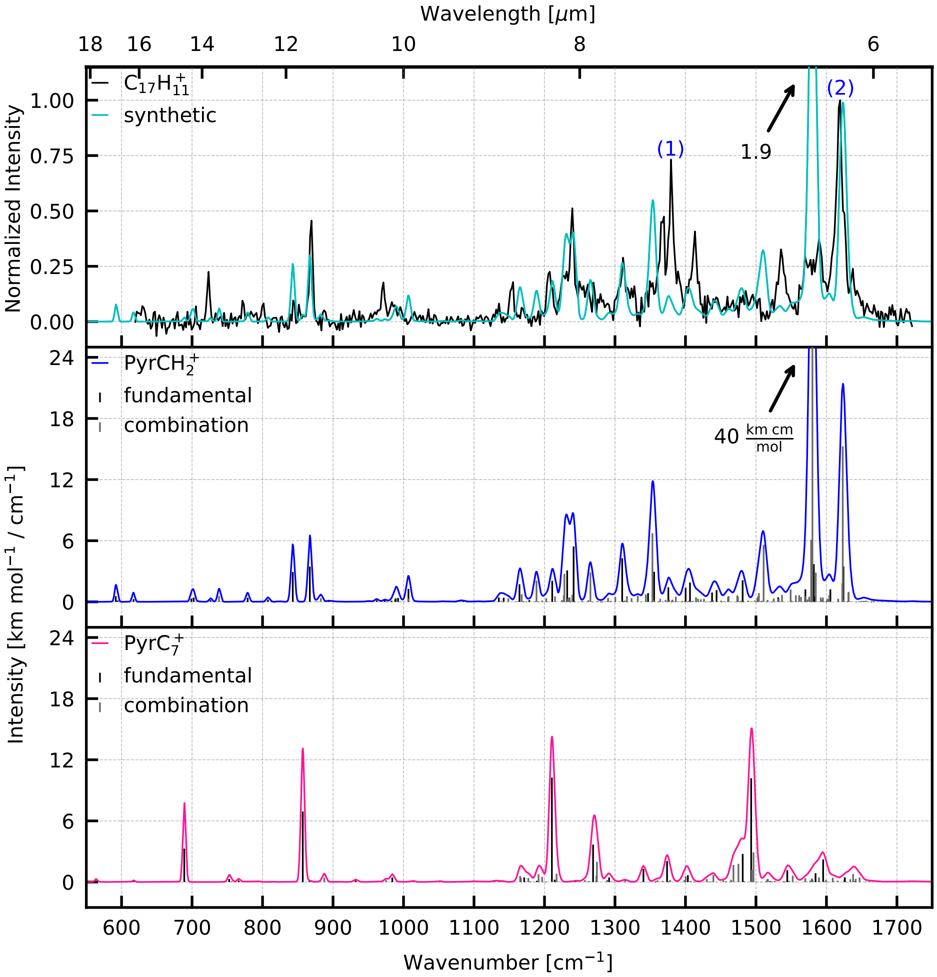

Figure 4: Experimental IRPD spectrum of the Ne-tagged $C_{17}H_{11}^+$ (top) compared to the calculated anharmonic IR spectra of the two considered isomers, $PyrCH_2^+$ (middle), and $PyrC_7^+$ (bottom) as computed using B3LYP/def2TZVPP. The cyan spectrum in the top panel corresponds to the synthetic spectrum that was generated from the two anharmonic spectra using the abundance ratio 0.95:0.05, as determined in Sect. 3.2.

complexity, which indicates the contribution of several isomers. On the basis of theoretical calculations, we could provide spectral evidence for XCH_2^+ in both cases, and evidence for XC_7^+ only in the case of X = Nap (see Sect. 3.3). This led us to consider other causes to account for the observed spectral complexity.

One might question the effect of Ne tagging on the spectra. To our knowledge no strong effect on the spectra of aromatic molecules has been reported. Some examples of calculated anharmonic spectra of the Ne tagged species using the same level of theory as for the bare ions are reported in Figs. S6 – S9 in the SM. These calculations indicate that there might be an effect of Ne tagging especially in the case of XCH_2^+ species in which the Ne atom is preferentially found in the molecular plane in interaction with the H atoms compared with XC_7^+ species for which the Ne atom is more often found out-of the molecular plane in interaction with the π electrons, which is a typical configuration for complexes of aromatic rings with rare gases [42, 43]. In the absence of experimental data on related reference systems, we cannot conclude on the accuracy of these calculations. This limits our ability to conclude on the presence of additional bare isomers than those that can be identified by specific spectral features.

A common spectral feature of our measurements is the strongest band of the IRPD spectra whose

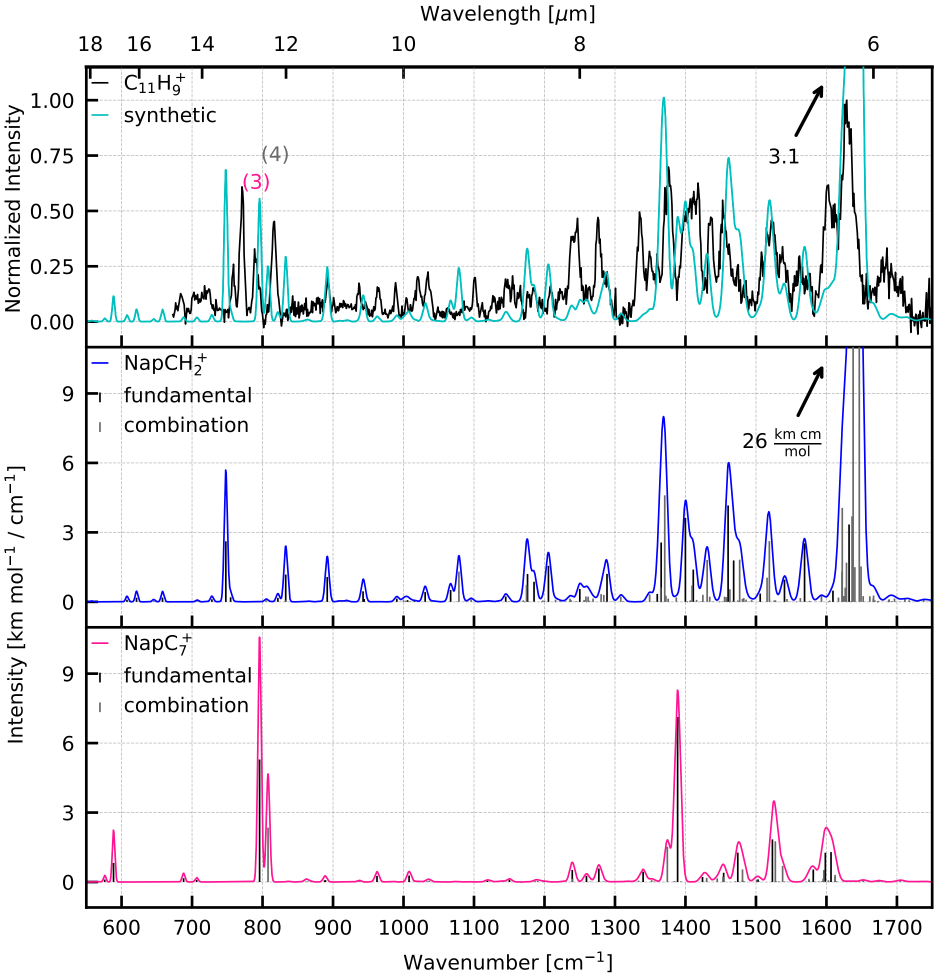

Figure 5: Experimental IRPD spectrum of the Ne-tagged $C_{11}H_9^+$ (top) compared to the calculated anharmonic IR spectra of the two considered isomers, $NapCH_2^+$ (middle), and $NapC_7^+$ (bottom) as computed using B3LYP/def2TZVPP. The cyan spectrum in the top panel corresponds to the synthetic spectrum that was generated from the two anharmonic spectra using the abundance ratio 0.7:0.3, as determined in Sect. 3.2.

intensity-weighted band position is at 1622, 1633, and 1606 cm^{-1} for $C_{17}H_{11}^+$, $C_{11}H_9^+$, and $C_{15}H_{11}^+$, respectively. We mainly attributed this band to the benzylium-like isomer, based on the theoretical spectra, but also in line with the IRPD spectrum of the benzylium cation presented in Jusko et al. [27]. These positions are found to be significantly blueshifted relative to the bare PAHs and PAH$^+$ [44]. This can be assigned to the perturbation of the aromatic ring by the $-CH_2$ group, as mentioned similarly in the case of protonated PAHs [45]. On the opposite, the aromaticity is maintained in the case of the tropylium-like isomers.

More detailed assignments based on the theoretical spectra of the non-tagged ions are provided in Tables S1 to S3 in the SM. As can be noted in these tables, the bands in the 1150 − 1650 cm^{-1} region are due to concerted in-plane CH bending (δ_{CH}) and CC stretching (ν_{CC}) modes, named $\delta_{CH} + \nu_{CC}$ hereafter. For the benzylium-like isomers, the main component of the lowest-energy $\delta_{CH} + \nu_{CC}$ intense modes involves the δ_{CH} of the $-CH_2$ group. Its position is calculated at 1582 cm^{-1} (6.32 μm), 1569 cm^{-1} (6.37 μm), and 1558 cm^{-1} (6.42 μm) for $PyrCH_2^+$, $NapCH_2^+$, and $AntCH_2^+$, respectively. The more delocalized and intense $\delta_{CH} + \nu_{CC}$ modes involve all the CH bonds of the molecules and are shifted towards higher energy. They can be found at 1624 cm^{-1} (6.16 μm),

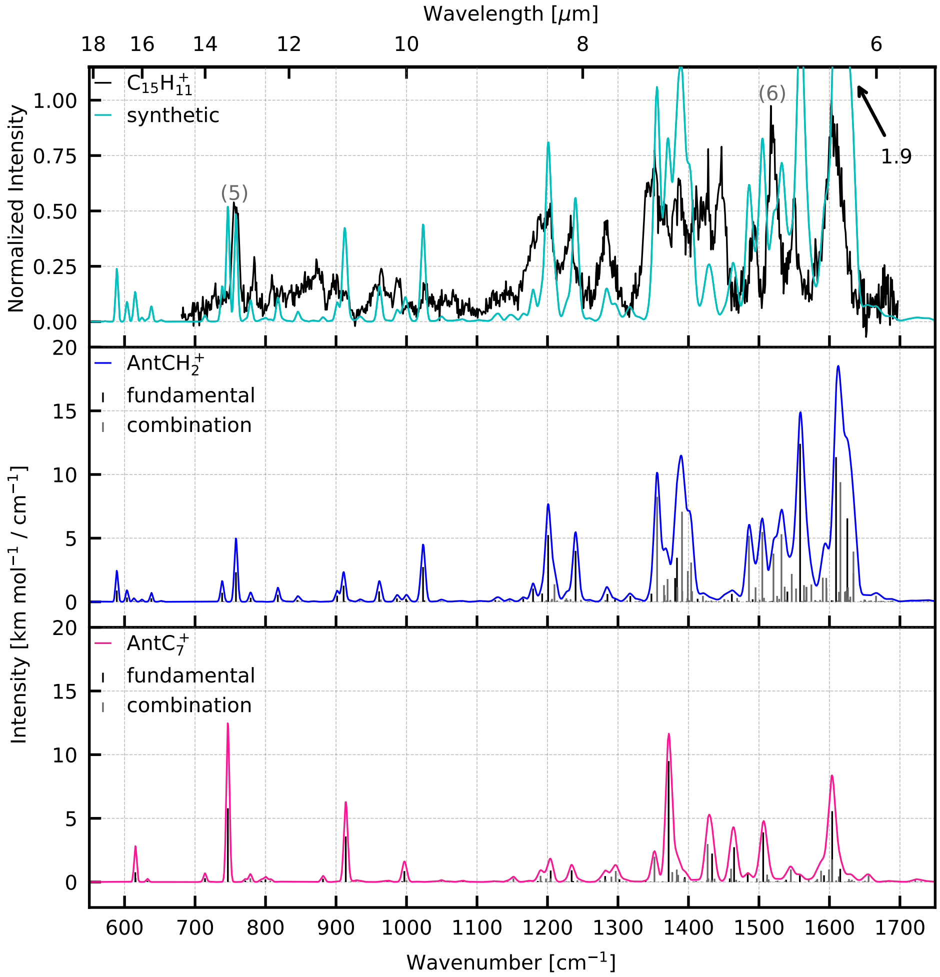

Figure 6: Experimental IRPD spectrum of the Ne-tagged $C_{15}H_{11}^+$ (top) compared to the calculated anharmonic IR spectra of the two considered isomers, $AntCH_2^+$ (middle), and $AntC_7^+$ (bottom) as computed using B3LYP/def2TZVPP. The cyan spectrum in the top panel corresponds to the synthetic spectrum that was generated from the two anharmonic spectra using the abundance ratio 0.7:0.3, as determined in Sect. 3.2.

1632 cm^{-1} (6.13 μm), and 1625 cm^{-1} (6.15 μm) in the cases of $PyrCH_2^+$, $NapCH_2^+$, and $AntCH_2^+$, respectively. Furthermore, some intense combination bands, that involve in particular some modes assigned to the $-CH_2$ group, are calculated above 1610 cm^{-1}, *i.e.*, 1623 cm^{-1} (6.16 μm) in the case of $PyrCH_2^+$, 1638 and 1647 cm^{-1} (6.11 and 6.07 μm) in the case of $NapCH_2^+$, and 1616 to 1634 cm^{-1} (6.19 to 6.12 μm) in the case of $AntCH_2^+$. We note that these combination bands tend to be too intense in the calculations, which is a known problem of perturbative methods such as VPT2 [46]. A clear example of this effect is seen in the case of $PyrCH_2^+$ for which there is a strong combination band at 1580 cm^{-1} (see Table S1 in the SM), that has no counterpart in the IRPD spectrum of $C_{17}H_{11}^+$. Still, it is very likely that these combination bands provide a significant contribution to the total intensities of the characteristic band of benzylium-like species at around 1600 cm^{-1}. The IRMPD spectrum of $C_{17}H_{11}^+$ was found to have no counterpart for the most intense band observed at 1622 cm^{-1} in the IRPD spectrum [28]. If combination bands are strongly involved, this might indeed account for this observation.

4.2. Considerations on chemical pathways

West et al. [29] computed the energetic profiles for the H loss from cationic 1-methylpyrene, $PyrCH_3^+$, leading to $PyrCH_2^+$ and $PyrC_7^+$. They

Table 1: Intensity-weighted band positions, $\bar{\nu}_i^{\mathrm{ex}}$, for each major band, i, observed in the IRPD spectra together with their respective integrated intensity, I_i^{ex}, and bandwidth, σ_i^{ex}, as determined by Eqs. (3) and (4). For comparison to the anharmonic IR spectra, the corresponding values for the synthetic spectra, $\bar{\nu}_i^{\mathrm{th}}$, I_i^{th}, and σ_i^{th}, and the difference between experimental and theoretical band positions, $\Delta\bar{\nu}_i$ according to Eq. (5), are also reported (see text for details).

	IRPD Spectrum			**B3LYP / def2TZVPP**				
	$C_{17}H_{11}^+$			**0.95 $PyrCH_2^+$ + 0.05 $PyrC_7^+$**				
Interval	$\bar{\nu}_i^{\mathrm{ex}}$ [cm^{-1}]	I_i^{ex}	σ_i^{ex} [cm^{-1}]	$\bar{\nu}_i^{\mathrm{th}}$ [cm^{-1}]	I_i^{th}	σ_i^{th} [cm^{-1}]	$\Delta\bar{\nu}_i$ [cm^{-1}]	**Notes**
[715 – 730]	723	1.1	2.1	726	0.1	2.2	-3	
[860 – 880]	869	2.7	2.4	867	2.1	3.2	1	
[1200 – 1215]	1207	2.0	3.0	1209	1.6	3.4	-2	
[1220 – 1245]	1234	5.7	6.0	1234	7.5	6.0	0	
[1295 – 1320]	1310	3.5	5.5	1310	3.2	5.1	0	
[1335 – 1395]	1371	14.5	13.2	1358	8.7	12.3	12	Band (1)
[1400 – 1425]	1412	4.7	5.2	1409	2.2	6.3	3	
[1525 – 1555]	1538	4.6	6.4	1541	1.9	8.8	-3	
[1555 – 1600]	1580	9.9	10.8	1580	26.3	6.9	1	
[1600 – 1655]	1622	17.0	10.9	1623	14.6	8.0	-1	Band (2)

	$C_{11}H_9^+$			**0.7 $NapCH_2^+$ + 0.3 $NapC_7^+$**				
Interval	$\bar{\nu}_i^{\mathrm{ex}}$ [cm^{-1}]	I_i^{ex}	σ_i^{ex} [cm^{-1}]	$\bar{\nu}_i^{\mathrm{th}}$ [cm^{-1}]	I_i^{th}	σ_i^{th} [cm^{-1}]	$\Delta\bar{\nu}_i$ [cm^{-1}]	**Notes**
[760 – 780]	770	4.8	3.7	765	0.0	5.7	5	
[780 – 800]	791	3.0	4.1	795	3.1	2.1	-5	Band (3)
[800 – 825]	816	4.1	3.6	809	1.9	5.4	7	Band (4)
[1230 – 1255]	1243	7.0	5.8	1245	1.6	6.6	-2	
[1270 – 1295]	1281	5.9	6.2	1285	3.1	5.7	-4	
[1325 – 1345]	1336	5.3	4.4	1339	0.3	4.0	-3	
[1365 – 1385]	1376	9.3	4.8	1372	11.1	4.7	4	
[1390 – 1425]	1408	15.4	8.8	1403	10.9	8.2	5	
[1430 – 1445]	1437	4.7	3.6	1434	2.0	3.2	3	
[1445 – 1485]	1462	10.4	10.2	1466	15.2	8.6	-5	
[1500 – 1550]	1525	13.5	12.0	1523	10.7	10.3	1	
[1585 – 1615]	1603	11.7	7.1	1603	4.1	7.8	0	
[1615 – 1660]	1633	21.8	9.6	1638	71.5	9.2	-6	

	$C_{15}H_{11}^+$			**0.7 $AntCH_2^+$ + 0.3 $AntC_7^+$**				
Interval	$\bar{\nu}_i^{\mathrm{ex}}$ [cm^{-1}]	I_i^{ex}	σ_i^{ex} [cm^{-1}]	$\bar{\nu}_i^{\mathrm{th}}$ [cm^{-1}]	I_i^{th}	σ_i^{th} [cm^{-1}]	$\Delta\bar{\nu}_i$ [cm^{-1}]	**Notes**
[745 – 770]	758	7.3	5.1	754	4.9	5.5	4	Band (5)
[1160 – 1210]	1189	17.7	12.8	1197	11.3	9.9	-8	
[1210 – 1250]	1230	10.5	10.1	1235	7.7	10.0	-5	
[1265 – 1310]	1285	10.4	10.3	1289	2.7	8.5	-3	
[1325 – 1460]	1393	63.7	37.1	1384	55.1	24.5	9	
[1485 – 1505]	1494	5.4	4.6	1495	10.0	6.3	-2	
[1505 – 1535]	1520	15.2	6.7	1520	15.7	9.1	0	Band (6)
[1535 – 1570]	1551	9.4	8.4	1555	27.4	8.9	-4	
[1575 – 1640]	1606	29.1	13.7	1614	58.9	13.5	-8	

found that the transition state (TS) of the rate determining step leading to the formation of PyrC_7^+ was 0.66 eV higher than the threshold for dissociation to PyrCH_2^+ [29]. In the present work, we considered similar mechanisms for the H loss for the three PAHs (see Fig. 7). They consist in -(i)- direct loss of H, for which we found no barrier on the double spin state surface leading to the benzylium-like isomer and -(ii)- a mechanism consisting of several steps inspired by West et al. [29] for the formation of the tropylium-like isomer. The first step is an H migration from the methyl group toward the closest C atom, followed by the migration of a CH_2 group toward the adjacent C atoms to form a kind of three-carbon ring. Finally, the C_7 ring is formed, and the H loss process leads to the tropylium-like isomer. For this last step, a TS was obtained (confirmed by IRC calculations) where the H atom leaves out-of-plane of the PAH (see $\mathrm{TS}^{(,\prime,\prime\prime)}_{4-\mathrm{trop}}$ in Fig. 7). In the case of 1-methylpyrene, we computed a similar TS as that published by West et al. [29] but with the H atom leaving orthogonally to the PAH plane. This TS was found 0.11 eV higher in energy than $\mathrm{PyrCH}_2^+ + \mathrm{H}$ at the DFT level of theory, and 0.30 eV at the CCSD(T) level.

For acene species, we expect a lower isomerization energy barrier leading to the tropylium-like isomer due to less geometrical constraint as compared to the pericondensed species. This is indeed illustrated by the calculated path presented in Fig. 7. In the case of naphthalene, the energy of the highest energy transition state leading to NapC_7^+ was found 2.74 eV above NapCH_3^+, which is 0.15 eV below the energy of $\mathrm{NapCH}_2^+ + \mathrm{H}$ at the B3LYP/6-31G(d,p) level of theory, and 0.13 eV higher after CCSD(T) single point calculations. This transition state involves a C_7 ring slightly distorted from planarity (with an angle for the CC bond involving the C atom that loses an H of 1.5 ° with respect to the PAH plane). The CCC internal angles of the C_7 ring lie in the range of 125.9 to 128.5 °, the smallest involving the common CC bond with the C_6 ring cycle. The transition state is less constrained than in the case of pyrene as the C_7 ring is only adjacent with one C_6 cycle against two in the case of pyrene. Similar results were obtained in the case of anthracene as the highest energy TS leading to AntC_7^+ was found 0.07 eV below the energy of $\mathrm{AntCH}_2^+ + \mathrm{H}$ at the DFT level, and +0.17 eV at the CCSD(T) level. Therefore, from a purely energetic point of view, the formation of both benzylium- and tropylium-like isomers are more favorable in the –H loss of 2-methylnaphthalene and 2-methylanthracene cations compared to the case of the 1-methylpyrene cation. This could be confirmed in our measurements for the naphthalene-derived species but not for the anthracene-derived species due to the observed spectral complexity as discussed in Sect. 4.1.

4.3. Astrophysical implications

Experiments under relevant astrophysical conditions have shown that methylated PAH cations are relatively easy to photodissociate but the formed –H fragments are almost as stable as the non-substituted parent species [23]. These species might therefore contribute to the AIB spectra, which calls for a better knowledge of their spectral signatures.

The most intense feature in our IRPD spectra is located around $1620\,\mathrm{cm}^{-1}$ ($6.17\,\mu$m). Peeters et al. [47] made a detailed study of this AIB feature from observations by the Infrared Space Observatory. They determined that, in the majority of objects, the $6.2\,\mu$m AIB peaks between 6.19 and $6.23\,\mu$m (called class A feature). It appeared clearly that this position is significantly blueshifted compared to the corresponding band in the IR spectra of bare PAHs [44, 48]. This led the authors to propose polycyclic aromatic nitrogen heterocycles (PANHs) as being the main carriers for this band. Other proposed carriers based on DFT calculations included PAH-metal ion complexes such as $[\mathrm{SiPAH}]^+$ π-complexes [49].

Recent progress in the assignment of the AIB at $6.2\,\mu$m came with a number of experiments on the IR spectroscopy of protonated PAHs using IRPD [50, 51] and IRMPD spectroscopy [52, 53], and more recently absorption spectroscopy in solid para-hydrogen matrices [45, 54, 55]. At the cold temperature of these matrices, bands are observed in the $1620\,\mathrm{cm}^{-1}$ range, which is very comparable to the values we obtained for XCH_2^+ species in IRPD spectroscopy. In the case of protonated ovalene, the largest protonated PAH studied so far, Tsuge et al. [45] pointed also to strong combination bands at 1650 and $1643\,\mathrm{cm}^{-1}$ (6.06 and $6.09\,\mu$m). These could contribute to the satellite band observed on the blue side of the $6.2\,\mu$m AIB. All these experiments point to protonated PAHs being attractive candidates to account for the AIB spectra. Our work shows that this is also the case of XCH_2^+. As discussed in Sect. 4.1, this can be accounted for in

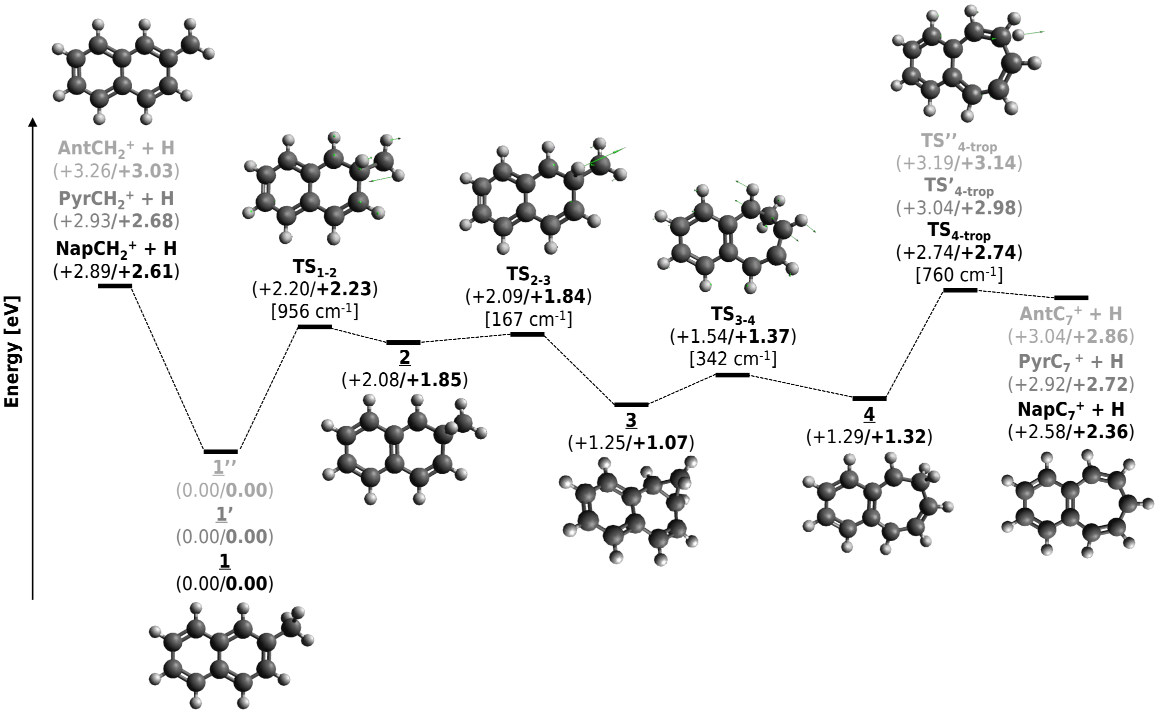

Figure 7: Computed energy profile (doublet spin state surface) for the H loss from $NapCH_3^+$ leading to $NapCH_2^+$ and $NapC_7^+$. The relative enthalpies at 0 K of the intermediates are indicated in eV in parentheses. Both B3LYP/6-31G(d,p) and CCSD(T)/6-311G(d,p)//B3LYP/6-31G(d,p) values are given, the latter in bold characters. The values for the intermediates of interest for the pyrene- and anthracene-like isomers are also indicated. Additionally, the corresponding B3LYP/6-31G(d,p) optimized geometries of the intermediates are reported for the $NapCH_3^+$ case. For transition states (TS), the norm of the negative wavenumber is indicated in square brackets.

both cases by the perturbation of the aromaticity of the substituted/protonated 6-carbon ring.

We expect that the conditions in PDRs where eVSGs of mixed aromatic and aliphatic composition interact with UV photons [8] are favorable for the formation of XCH_2^+ species. The latter can be produced upon the absorption of one or two UV photons starting from methylated or ethylated PAHs. Jochims et al. [22] demonstrated that for methylnaphthalene and methylanthracene, this can happen upon the absorption of a single UV photon of energy less than 13.6 eV. Marciniak et al. [23] observed the formation of the –H fragment starting from the parent cations for larger PAHs (up to 24 carbon atoms) using a single photon energy of 10.5 eV. This is not sufficient to derive a dissociation threshold but demonstrates that the two-step process to form XCH_2^+ is feasible as well.

5. Conclusions

We have performed IRPD spectroscopy in order to characterize the species produced in the –H dissociative ionization of methylated PAHs, as well as their spectral signatures. The recorded IRPD spectra show that the strongest band is located at about $1620\,cm^{-1}$, which points to a dominant contribution of the benzylium-like isomer, XCH_2^+. From depletion measurements, we concluded that at least two isomers are present in significant fraction in the case of acene-derived species, whereas essentially one is present for the more compact PAH, $C_{17}H_{11}^+$. A second expected isomer based on energetic consideration is the tropylium-like isomer, XC_7^+. Its presence in the acene-derived species but not in the more compact pyrene-derived species could be predicted due to a lower isomerization energy barrier in the formation of tropylium-like isomers with respect to the energy necessary to form the benzylium-like isomer. The relative abundances derived from saturation depletion measurements were used to generate a synthetic spectrum using theoretical anharmonic IR spectra of the two lowest-energy isomers, XCH_2^+ and XC_7^+. Direct spectral evidence for the tropylium-like isomer was found only for the smallest investigated species, $NapC_7^+$, with a maximum relative abundance of approximately 40 % derived from depletion measurements.

We found that the synthetic spectra were not able to account for the full observed spectral complexity, which is especially true in the case of the acene-derived species. This suggests the presence of additional isomers at higher energy compared to XCH_2^+ and XC_7^+. However, we could not reveal the presence of additional isomers from spectral analysis. This is due to the lack of validation for the calculated anharmonic spectra. The same applies to elaborating on a possible contribution of Ne tagging to the molecular complexity. Further investigations are needed both from the theoretical and experimental sides to conclude on this point.

From an astrophysical perspective, our study suggests that XCH_2^+ species are attractive candidates to account for the $6.2\,\mu$m AIB. It also shows that a significant fraction of tropylium-like isomers are not expected to be found in astrophysical environments where methylated PAHs are submitted to UV photons. These could only be formed at a maximum relative abundance of about 40 % for (small) catacondensed PAHs. Further isomerization upon UV irradiation is, however, not excluded which could lead to a fraction of species of tropylium-like isomers even for more compact PAHs. Indeed, in their theoretical investigations, Rapacioli et al. [25] found four pathways with barrier heights of $3.5 - 4$ eV for the isomerization process between $PyrCH_2^+$ and $PyrC_7^+$. This barrier could be overcome in astrophysical environments where PAHs are continuously photoprocessed. However, this possibility remains yet to be tested in the laboratory.

CRediT authorship contribution statement

Gabi Wenzel: Conceptualization, Software, Formal analysis, Investigation, Data curation, Writing – original draft, Writing – review & editing, Visualization, Funding acquisition. **Aude Simon:** Software, Investigation, Validation, Resources, Data curation, Writing – original draft, Writing – review & editing. **Shreyak Banhatti:** Software, Investigation. **Pavol Jusko:** Software, Validation, Investigation, Writing – review & editing. **Stephan Schlemmer:** Resources, Writing – review & editing, Supervision, Funding acquisition. **Sandra Brünken:** Conceptualization, Validation, Investigation, Resources, Writing – review & editing, Supervision, Funding acquisition. **Christine Joblin:** Conceptualization, Validation, Resources, Data curation, Writing – original draft, Writing – review & editing, Supervision, Project administration, Funding acquisition.

Declaration of competing interest

The authors declare that they have no known competing financial interests or personal relationships that could have appeared to influence the work reported in this paper.

Dataset

The dataset associated with this work can be found under `https://doi.org/10.5281/zenodo.5729322`.

Acknowledgements

We would like to thank the two anonymous reviewers for their careful reading and their thoughtful comments and suggestions that helped us to improve the quality of this paper. We gratefully acknowledge the support of Radboud University and the Dutch Research Council (NWO) for providing the required beam time at the FELIX Laboratory. We are grateful to the staff from FELIX for the smooth running of the facility. The research leading to these results was supported by the funding received from LASERLAB-EUROPE, Grant Agreement no. 654148, under the European Union's (EU) Horizon 2020 research and innovation programme. We also acknowledge funding from the European Research Council under the EU's Seventh Framework Programme (FP/2007-2013) ERC-2013-SyG, Grant Agreement no. 610256 NANOCOSMOS. G. W. and Sh. B. thank the EU for support under the Horizon 2020 framework for the Marie Skłodowska-Curie action EUROPAH, Grant Agreement no. 722346. A. S. thanks the computing mesocenter CALMIP ("CALcul en MIdi Pyrénées", UMS CNRS 3667) for generous allocation of computer resources.

Appendix A. Supplementary data

Supplementary material related to this article can be found online at `https://doi.org/10.1016/j.jms.2022.111620`.

References

[1] A. Tielens, Annual Review of Astronomy and Astrophysics 46 (2008) 289–337. doi:10.1146/annurev.astro.46.060407.145211.

[2] M. Rapacioli, C. Joblin, P. Boissel, A&A 429 (2005) 193–204. doi:10.1051/0004-6361:20041247.

[3] O. Berné, C. Joblin, Y. Deville, J. D. Smith, M. Rapacioli, J. P. Bernard, J. Thomas, W. Reach, A. Abergel, A&A 469 (2007) 575–586. doi:10.1051/0004-6361:20066282.

[4] P. Pilleri, J. Montillaud, O. Berné, C. Joblin, A&A 542 (2012) A69. doi:10.1051/0004-6361/201015915.

[5] R. Visser, V. C. Geers, C. P. Dullemond, J.-C. Augereau, K. M. Pontoppidan, E. F. van Dishoeck, A&A 466 (2007) 229–241. doi:10.1051/0004-6361:20066829.

[6] J. Montillaud, C. Joblin, D. Toublanc, A&A 552 (2013) A15. doi:10.1051/0004-6361/201220757.

[7] H. Andrews, C. Boersma, M. W. Werner, J. Livingston, L. J. Allamandola, A. G. G. M. Tielens, ApJ 807 (2015) 99. doi:10.1088/0004-637X/807/1/99.

[8] P. Pilleri, C. Joblin, F. Boulanger, T. Onaka, A&A 577 (2015) A16. doi:10.1051/0004-6361/201425590.

[9] J. Shan, M. Suton, L. C. Lee, The Astrophysical Journal 383 (1991) 459. doi:10.1086/170803.

[10] C. Joblin, A. G. G. M. Tielens, L. J. Allamandola, T. R. Geballe, The Astrophysical Journal 458 (1996) 610. doi:10.1086/176843.

[11] F. Pauzat, D. Talbi, Y. Ellinger, Monthly Notices of the Royal Astronomical Society 304 (1999) 241–253. doi:10.1046/j.1365-8711.1999.02240.x.

[12] X. J. Yang, A. Li, R. Glaser, J. X. Zhong, ApJ 825 (2016) 22. doi:10.3847/0004-637X/825/1/22.

[13] M. Schuhmann, K. Altwegg, H. Balsiger, J.-J. Berthelier, J. De Keyser, B. Fiethe, S. A. Fuselier, S. Gasc, T. I. Gombosi, N. Hänni, M. Rubin, C.-Y. Tzou, S. F. Wampfler, Astronomy and Astrophysics 630 (2019) A31. doi:10.1051/0004-6361/201834666.

[14] M. H. Studier, R. Hayatsu, E. Anders, Science 149 (1965) 1455–1459. doi:10.1126/science.149.3691.1455.

[15] B. P. Basile, B. S. Middleditch, J. Oró, Organic Geochemistry 5 (1984) 211–216. doi:10.1016/0146-6380(84)90008-1.

[16] J. E. Elsila, N. P. de Leon, P. R. Buseck, R. N. Zare, Geochimica et Cosmochimica Acta 69 (2005) 1349–1357. doi:10.1016/j.gca.2004.09.009.

[17] H. Sabbah, A. Bonnamy, D. Papanastasiou, J. Cernicharo, J.-A. Martín-Gago, C. Joblin, ApJ 843 (2017) 34. doi:10.3847/1538-4357/aa73dd.

[18] M. Blumer, W. W. Youngblood, Science 188 (1975) 53–55. doi:10.1126/science.188.4183.53.

[19] B. Shukla, A. Miyoshi, M. Koshi, Journal of the American Society for Mass Spectrometry 21 (2010) 534–544. doi:10.1016/j.jasms.2009.12.019.

[20] L. G. Marin, S. Bejaoui, M. Haggmark, N. Svadlenak, M. de Vries, E. Sciamma-O'Brien, F. Salama, ApJ 889 (2020) 101. doi:10.3847/1538-4357/ab62b7.

[21] G. Santoro, L. Martínez, K. Lauwaet, M. Accolla, G. Tajuelo-Castilla, P. Merino, J. M. Sobrado, R. J. Peláez, V. J. Herrero, I. Tanarro, Á. Mayoral, M. Agúndez, H. Sabbah, C. Joblin, J. Cernicharo, J. Á. Martín-Gago, ApJ 895 (2020) 97. doi:10.3847/1538-4357/ab9086.

[22] H. W. Jochims, H. Baumgärtel, S. Leach, ApJ 512 (1999) 500. doi:10.1086/306752.

[23] A. Marciniak, C. Joblin, G. Mulas, V. R. Mundlapati, A. Bonnamy, A&A 652 (2021) A42. doi:10.1051/0004-6361/202140737.

[24] R. C. Dunbar, J. Am. Chem. Soc. 97 (1975) 1382–1384. doi:10.1021/ja00839a016.

[25] M. Rapacioli, A. Simon, C. C. M. Marshall, J. Cuny, D. Kokkin, F. Spiegelman, C. Joblin, J. Phys. Chem. A 119 (2015) 12845–12854. doi:10.1021/acs.jpca.5b09494.

[26] B. Chiavarino, M. E. Crestoni, O. Dopfer, P. Maitre, S. Fornarini, Angewandte Chemie International Edition 51 (2012) 4947–4949. doi:10.1002/anie.201200558.

[27] P. Jusko, A. Simon, S. Banhatti, S. Brünken, C. Joblin, ChemPhysChem 19 (2018) 3182–3185. doi:10.1002/cphc.201800744.

[28] P. Jusko, A. Simon, G. Wenzel, S. Brünken, S. Schlemmer, C. Joblin, Chemical Physics Letters 698 (2018) 206–210. doi:10.1016/j.cplett.2018.03.028.

[29] B. West, B. Lowe, P. M. Mayer, J. Phys. Chem. A 122 (2018) 4730–4735. doi:10.1021/acs.jpca.8b02667.

[30] P. Jusko, S. Brünken, O. Asvany, S. Thorwirth, A. Stoffels, L. van der Meer, G. Berden, B. Redlich, J. Oomens, S. Schlemmer, Faraday Discuss. 217 (2019) 172–202. doi:10.1039/C8FD00225H.

[31] D. Oepts, A. F. G. van der Meer, P. W. van Amersfoort, Infrared Physics & Technology 36 (1995) 297–308. doi:10.1016/1350-4495(94)00074-U.

[32] D. Gerlich, in: Advances in Chemical Physics, John Wiley & Sons, Ltd, 1992, pp. 1–176. doi:10.1002/9780470141397.ch1.

[33] S. Banhatti, J. Palotás, P. Jusko, B. Redlich, J. Oomens, S. Schlemmer, S. Brünken, A&A 648 (2021) A61. doi:10.1051/0004-6361/202039744.

[34] S. Brünken, F. Lipparini, A. Stoffels, P. Jusko, B. Redlich, J. Gauss, S. Schlemmer, J. Phys. Chem. A 123 (2019) 8053–8062. doi:10.1021/acs.jpca.9b06176.

[35] A. N. Marimuthu, D. Sundelin, S. Thorwirth, B. Redlich, W. D. Geppert, S. Brünken, Journal of Molecular Spectroscopy 374 (2020) 111377. doi:10.1016/j.jms.2020.111377.

[36] C. Joblin, G. Wenzel, S. R. Castillo, A. Simon, H. Sabbah, A. Bonnamy, D. Toublanc, G. Mulas, M. Ji, A. Giuliani, L. Nahon, J. Phys.: Conf. Ser. 1412 (2020) 062002. doi:10.1088/1742-6596/1412/6/062002.

[37] T. Heine, M. Rapacioli, J. Cuny, S. Patchkovskii, J. Frenzel, A. Koster, P. Calaminici, H. A. Duarte, S. Escalante, R. Flores-Moreno, A. Goursot, J. Reveles, D. Salahub, A. Vela, deMonNano, `http://demon-nano.ups-tlse.fr/` (2009).

[38] M. J. Frisch, G. W. Trucks, H. B. Schlegel, G. E. Scuseria, M. A. Robb, J. R. Cheeseman, G. Scalmani, V. Barone, G. A. Petersson, H. Nakatsuji, X. Li, M. Caricato, A. V. Marenich, J. Bloino, B. G. Janesko, R. Gomperts, B. Mennucci, H. P. Hratchian, J. V. Ortiz, A. F. Izmaylov, J. L. Sonnenberg, D. Williams-Young, F. Ding, F. Lipparini, F. Egidi, J. Goings, B. Peng, A. Petrone, T. Henderson, D. Ranasinghe, V. G. Zakrzewski, J. Gao, N. Rega, G. Zheng,

W. Liang, M. Hada, M. Ehara, K. Toyota, R. Fukuda, J. Hasegawa, M. Ishida, T. Nakajima, Y. Honda, O. Kitao, H. Nakai, T. Vreven, K. Throssell, J. A. Montgomery, Jr., J. E. Peralta, F. Ogliaro, M. J. Bearpark, J. J. Heyd, E. N. Brothers, K. N. Kudin, V. N. Staroverov, T. A. Keith, R. Kobayashi, J. Normand, K. Raghavachari, A. P. Rendell, J. C. Burant, S. S. Iyengar, J. Tomasi, M. Cossi, J. M. Millam, M. Klene, C. Adamo, R. Cammi, J. W. Ochterski, R. L. Martin, K. Morokuma, O. Farkas, J. B. Foresman, D. J. Fox, Gaussian 16 Revision B.01, Gaussian Inc. Wallingford CT, 2016.

[39] V. Barone, J. Chem. Phys. 122 (2005) 014108. doi:10.1063/1.1824881.

[40] F. Weigend, R. Ahlrichs, Phys. Chem. Chem. Phys. 7 (2005) 3297–3305. doi:10.1039/B508541A.

[41] S. Chakraborty, G. Mulas, M. Rapacioli, C. Joblin, Journal of Molecular Spectroscopy 378 (2021) 111466. doi:10.1016/j.jms.2021.111466.

[42] T. Brupbacher, J. Makarewicz, A. Bauder, J. Chem. Phys. 101 (1994) 9736–9746. doi:10.1063/1.467939.

[43] A. Maris, W. Caminati, P. G. Favero, Chemical Communications 0 (1998) 2625–2626. doi:10.1039/A807289B.

[44] D. M. Hudgins, C. W. Bauschlicher Jr., L. J. Allamandola, The Astrophysical Journal 632 (2005) 316–332. doi:10.1086/432495.

[45] M. Tsuge, M. Bahou, Y.-J. Wu, L. Allamandola, Y.-P. Lee, ApJ 825 (2016) 96. doi:10.3847/0004-637X/825/2/96.

[46] G. Mulas, C. Falvo, P. Cassam-Chenaï, C. Joblin, J. Chem. Phys. 149 (2018) 144102. doi:10.1063/1.5050087.

[47] E. Peeters, S. Hony, C. V. Kerckhoven, A. G. G. M. Tielens, L. J. Allamandola, D. M. Hudgins, C. W. Bauschlicher, A&A 390 (2002) 1089–1113. doi:10.1051/0004-6361:20020773.

[48] C. Boersma, J. D. Bregman, L. J. Allamandola, ApJ 769 (2013) 117. doi:10.1088/0004-637X/769/2/117.

[49] B. Joalland, A. Simon, C. J. Marsden, C. Joblin, A&A 494 (2009) 969–976. doi:10.1051/0004-6361:200810863.

[50] G. E. Douberly, A. M. Ricks, P. v. R. Schleyer, M. A. Duncan, J. Phys. Chem. A 112 (2008) 4869–4874. doi:10.1021/jp802020n.

[51] A. M. Ricks, G. E. Douberly, M. A. Duncan, ApJ 702 (2009) 301–306. doi:10.1088/0004-637X/702/1/301.

[52] U. J. Lorenz, N. Solcà, J. Lemaire, P. Maître, O. Dopfer, Angewandte Chemie International Edition 46 (2007) 6714–6716. doi:10.1002/anie.200701838.

[53] H. Knorke, J. Langer, J. Oomens, O. Dopfer, ApJ 706 (2009) L66–L70. doi:10.1088/0004-637X/706/1/L66.

[54] M. Bahou, Y.-J. Wu, Y.-P. Lee, J. Phys. Chem. Lett. 4 (2013) 1989–1993. doi:10.1021/jz400923k.

[55] M. Bahou, Y.-J. Wu, Y.-P. Lee, Angewandte Chemie 126 (2014) 1039–1042. doi:10.1002/ange.201308971.